Electronic energies, geometries, and vibrational frequencies of the ground and low-lying excited states of the boron trimer

Ramon Hernandez and Jack Simons
Chemistry Department, University of Utah, Salt Lake City, Utah 84112

(Received 10 September 1990; accepted 19 November 1990)

Ab initio electronic structure calculations on several low-lying valence states of B_3 have been carried out using correlation-consistent polarized valence double-zeta basis sets and complete-active-space self-consistent field treatments of electron correlation. Stable triangular structures, linear structures, and Jahn–Teller unstable structures are all observed. Equilibrium geometries, energies, and local harmonic vibrational frequencies are determined for various locally stable structures of several states. Several of the local minima are found to be unstable or metastable when zero-point vibrational energy is included; as a result, fluxional species are predicted to occur for certain B_3 states. Transition states connecting local minima are found and characterized in terms of energies, geometries, and local harmonic vibrational frequencies. The ground state of B_3 is predicted to have an equilateral triangular structure and to be of $^2A_1'$ symmetry in the D_{3h} point group. Dipole and vibronically allowed vertical transition energies to other states are also considered.

I. INTRODUCTION

Over the past several years there has been growing interest in the structures and energetics of small clusters of atoms and ions involving both main-group elements and transition elements. Relative electronic energies, equilibrium geometries, and vibrational frequencies, as well as dissociation energies and isomerization energies are features that are of particular interest. In this study, such information has been determined for several low-lying bent, triangular, and linear states of the boron trimer B_3, using *ab initio* quantum chemistry techniques. The boron trimer has not been spectroscopically observed but boron cluster cations were studied recently in collision induced dissociation experiments.[1] Also, electronic transitions in the aluminum trimer were recently characterized[2] using resonance enhanced multiphoton ionization (REMPI) techniques. It is our hope that the present work will motivate a similar study of the boron trimer.

Two especially interesting and relevant characteristics of the boron trimer's potential energy surfaces (PES) were examined as part of this study: (a) States that are symmetry degenerate at D_{3h} geometry are subject to first-order Jahn–Teller distortion (FOJT). For these states, we followed the FOJT distortion to locate minima on the corresponding double-cone surfaces as well as saddle points connecting these minima. The energy differences between the minima and the saddles, the barriers to pseudorotation, are also characterized. (b) For the nonspatially degenerate $^2A_1'$ ground state, which has an equilateral triangle equilibrium structure, rearrangement to a higher energy but still geometrically stable linear structure, was examined. Along this path, a barrier was found and characterized in terms of geometry, energy, and vibrational frequencies. This barrier is found to lie low enough in relation to the zero-point corrected energy of the linear structure to render the linear structure dynamically metastable.

The relevance of the findings of this work to future experimental spectroscopic studies is analyzed. Also, comparison with the results of earlier theoretical research on B_3 is presented.

II. METHODOLOGY

A. Atomic orbital basis sets

The basis set for the boron atoms uses Dunning's correlation-consistent polarized valence double-zeta (CC-pVDZ) $[9s4p1d|3s2p1d]$ basis.[3] This basis contains 45 functions for the boron trimer. To further test its adequacy, we performed calculations on the ground and first excited state of the boron dimer. Equilibrium bond lengths, harmonic frequencies, and the electronic term energies for the two states involved were obtained. Direct comparison with experiment[4] can be made only for the ground state. For the first excited state, we can compare our results to the accurate theoretical values of Dupuis and Liu.[5] As can be seen from Table I, good agreement is obtained for both of these B_2 states.

B. Electronic configurations

For the boron dimer, complete-active-space self-consistent field (CASSCF) calculations were performed. In these calculations, we doubly occupied the $1\sigma_g$, $2\sigma_g$, and $1\sigma_u$ orbitals in each configuration and the remaining four electrons were distributed, in all possible ways consistent with overall space and spin symmetry, among the active valence $2\sigma_u$, $1\pi_u$, $1\pi_g$, $3\sigma_g$ orbitals.

For the boron trimer an analogous partitioning was carried out. The $1a_1$, $2a_1$, $3a_1$, $1b_2$ orbitals were doubly occupied in all configurations, and the remaining seven electrons were distributed, in all possible ways consistent with overall space and spin symmetry, among the active $4a_1$, $5a_1$, $6a_1$, $1a_2$, $1b_1$, $2b_1$, $2b_2$, $3b_2$, $4b_2$ orbitals. The high energy $7a_1$ and $5b_2$ orbitals are not occupied in any of the configurations. This choice generates more than 9800 configurations of doublet and quartet spin symmetry. The adequacy of the active space selection for the dimer was confirmed by com-

 0021-9606/91/042961-07$03.00

TABLE I. Equilibrium bond lengths, harmonic frequencies, and electronic term energies for the ground and first excited states of B_2.

States	Property	CASSCF	DL[a]	Exp[b]
$1\,^3\Sigma_g^-$	r_e (Å)	1.598	1.620	1.590
$1\,^5\Sigma_u^-$	r_e (Å)	1.559	1.546	···
$1\,^3\Sigma_g^-$	ω_e (cm^{-1})	1094	988	1035
$1\,^5\Sigma_u^-$	ω_e (cm^{-1})	1221	1204	···

Term energies (T_e in cm^{-1})

Transition	MRCI[c]	DL[a]
$1\,^5\Sigma_u^- \rightarrow 1\,^3\Sigma_g^-$	1391	1271

[a] Theoretical results of Dupuis and Liu. See Ref. 5.
[b] Experimental results from Ref. 4.
[c] Refers to this work's multireference configuration interaction result.

paring calculated properties with experimental and previous theoretical results as discussed above. For the trimer, we carried out a series of exploratory calculations varying the active space until we found a compact space that describes the low-lying states in the energy region of interest to a precision that was relatively unchanged when additional configurations were included.

C. Geometry optimization

Searching for the minima and transition states on the three-dimensional potential energy surfaces of the low-lying states of the boron trimer would not have been feasible in the absence of an automated surface walking algorithm. In arriving at the results presented here, we employed our own surface walking algorithm which is detailed elsewhere.[6] This procedure (1) uses local first and second derivative data (to move toward or away from local minima), (2) takes "steps" of (variable) length determined by the accuracy of the local quadratic approximation to the actual energy surface, (3) maps out "streambeds" which connect local minima through transition states. Our Utah MESS-KIT modular electronic structure codes[7] generate the CASSCF analytical energy derivative data used as input for making use of this walking algorithm.

III. CHARACTERISTICS OF LOW-LYING STATES

A. Orbital correlation diagram

A qualitative picture of the electronic structure of the low-lying valence states of B_3 can be obtained from the molecular orbital (MO) correlation diagram shown in Fig. 1. In this diagram we describe the valence molecular orbitals (arising from the atomic $2s$ and $2p$ orbitals) at three nominal geometries: linear ($D_{\infty h}$), bent (C_{2v}), and equilateral triangular (D_{3h}) (for future use, a listing of the connections among the irreducible representations for these three symmetries is given in Table II). Because C_{2v} symmetry is preserved along paths connecting linear, bent, and triangular geometries, C_{2v} symmetry labels are used throughout Fig. 1. Doing so allows one to correlate orbitals along C_{2v}—preserving deformations and ultimately to establish correlations among electronic configurations and states at the different geometries. These exercises are, of course, of great

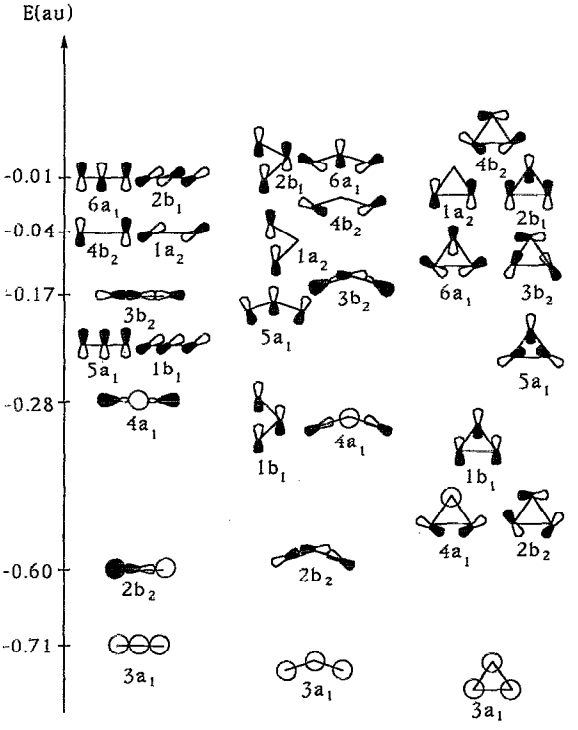

FIG. 1. Molecular orbital correlation diagram at three nominal geometries: equilateral triangular, bent, and linear. The C_{2v} point group symmetry labels are used for all geometries.

help in understanding the pattern of low-lying states that our *ab initio* calculations produce at various geometries.

All of the states considered in this study arise from different occupation of the $3a_1$, $(4a_1, 2b_2)$, $1b_1$, $5a_1$, $(6a_1, 3b_2)$, $(1a_2, 2b_1)$, and $4b_2$ orbitals shown in Fig. 1 (the parentheses are used to group orbitals that are degenerate at D_{3h} geometries); as such, they are all valence states. Because each boron atom has 4 valence orbitals and only 3 valence electrons, there are a large number of low-energy configurations that can be formed by distributing the 9 valence electrons among the 12 valence MOs. As stated earlier, the $3a_1$ orbital was doubly occupied and the $7a_1$ and $5b_2$ orbitals were entirely unoccupied in all of the calculations whose results are detailed here. Even so, more than 9800 configurations arise. The challenge of this high state density and the resultant richness of electronic spectral features is one of the reasons we decided to examine this particular species.

TABLE II. Correlations among irreducible representations of $D_{\infty h}$, D_{3h}, and C_{2v} symmetry.

$D_{\infty h}$	C_{2v}	D_{3h}	C_{2v}
Π_u	$A_1 + B_1$	A_1'	A_1
Π_g	$A_2 + B_2$	E'	A_1
Σ_u^-	A_2	A_1''	A_2
Σ_g^-	B_1	E''	A_2
Δ_u	$A_2 + B_2$	A_2''	B_1
		E''	B_1
		A_2'	B_2
		E'	B_2

B. Classification of states as nondegenerate triangular states, degenerate states that distort, and linear states

All of the low-lying valence states that we examined can be grouped into three categories: (1) Spatially nondegenerate states that have stable structures at an equilateral-triangle geometry. (2) Spatially doubly degenerate states (at D_{3h} geometry) that are, therefore, subject to first-order Jahn–Teller (FOJT) distortion [see Fig. 2(a)]. Following the lowest energy member of each such a pair of states along a distortion in one direction leads to a bent minimum [e.g., such as that labeled A in Fig. 2(b)]; distortion in the opposite direction, leads to a stationary point that is a transition state [labeled B in Fig. 2(b)]. On this lower-energy surface, there are three equivalent sets of such minima and transition states; these minima and saddle points are connected by paths that do not preserve overall C_{2v} symmetry. For each such lower-energy surface, there is also a higher-energy surface that results from deformation of the doubly degenerate D_{3h} state; these higher-energy surfaces were not examined in this work. (3) States that have stable linear $D_{\infty h}$ geometries; these states, in turn, connect with various states from categories (1) and (2). Among all the states examined, none were found to possess stable geometries of lower than C_{2v} symmetry.

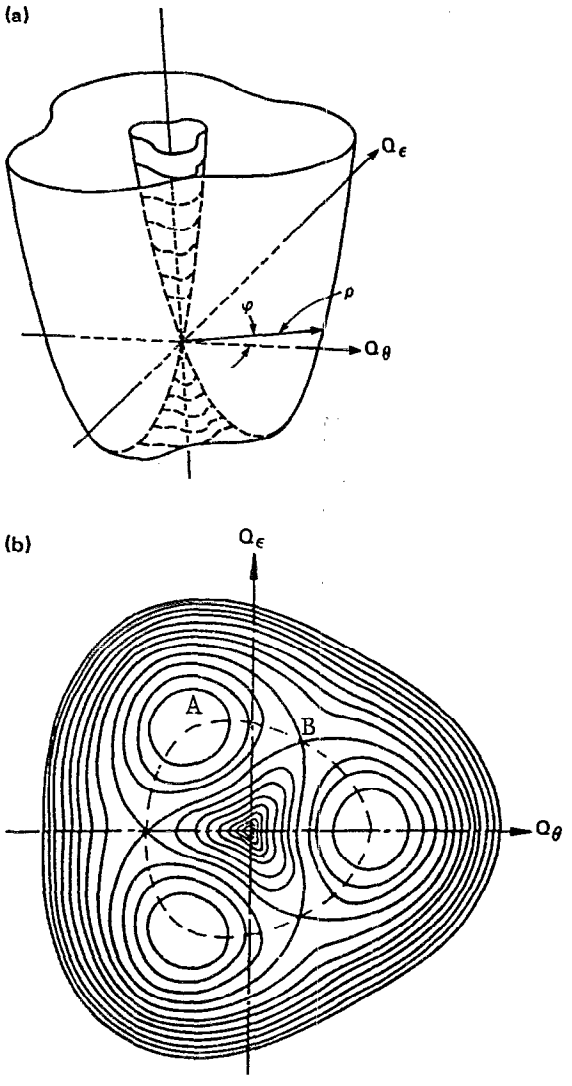

FIG. 2. (a) Double-cone potential energy surface characteristic of first-order Jahn–Teller species. The Cartesian coordinates can be thought of as the bending and asymmetric vibrational modes. (b) Contour map of the lower sheet in the double-cone surface. The threefold minima and saddle points are shown.

C. Overview of relative state energies and state correlation diagram

An overview of the low-lying states of B_3, as obtained in our *ab initio* calculations, is given in Fig. 3; there are 15 states having triangle or bent structures lying within 30 000 cm^{-1} of the triangular $1\,^2A_1'$ ground state. States in category (1) are placed to the left, category (2) states appear at the center and category (3) states are to the right. Correlations among these states are shown by the solid connecting lines. For the triangular states (which are geometrically stable in D_{3h} geometry) and the bent states (which arose by distorting degenerate D_{3h} structures), we give the D_{3h} term symbol labels to keep track of their D_{3h} parentage. The bent states that arise from symmetry-degenerate states are represented by two crossing curves to emphasize that there are two relevant electronic states appearing in a double-cone intersection [see Fig. 2(a)].

IV. RESULTS OF CALCULATIONS OF GEOMETRIES, ENERGIES, AND VIBRATIONAL FREQUENCIES

A. The ground and other spatially nondegenerate states

The basic structural and energetic features of the low-lying states of B_3 are summarized in Tables III(A) and

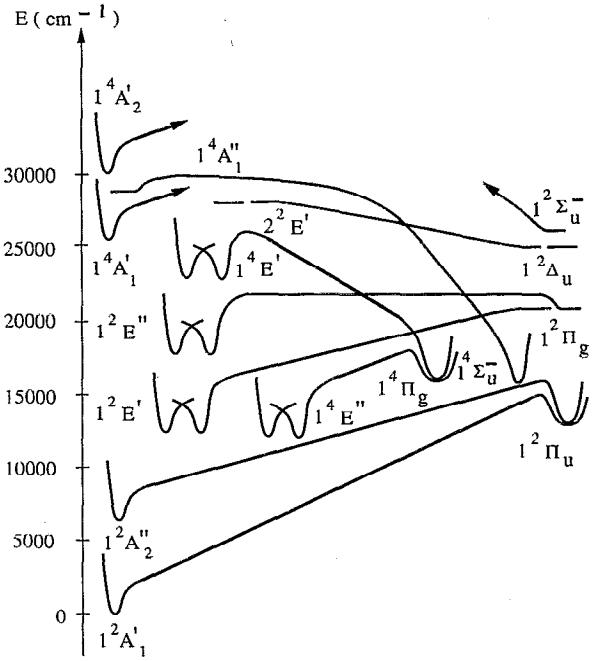

FIG. 3. Overview picture of the low-lying states in B_3. The different curves represent states that have been geometrically optimized. The horizontal lines represent states for which electronic energies are known but whose geometry has not been optimized.

TABLE III(A). Equilibrium geometries, harmonic frequencies, and electronic energies for low-lying bent states of B_3. (B). Equilibrium geometries, harmonic frequencies, and electronic energies for low-lying linear states of B_3.

A States[a]	r_e (Å)	θ	ω_s	ω_a	ω_b (cm^{-1})[b]	E (a.u.)
$1\,^2A_1'(1\,^2A_1)$	1.587	60.0	1214	869	869	−73.906 715
$1\,^2A_2''(1\,^2B_1)$	1.617	60.0	1176	828	828	−73.875 377
$1\,^4E''(1\,^4A_2)$	1.607	70.4	1083	951	533	−73.850 665
$1\,^4E''(1\,^4B_1)$	1.714	55.8	1091	1055i[c]	916	−73.846 669
$1\,^2E'(1\,^2B_2)$	1.598	65.3	1119	922	612	−73.850 665
$1\,^2E'(2\,^2A_1)$	1.657	57.2	1134	1032i[c]	928	−73.849 540
$1\,^2E''(1\,^2A_2)$	1.603	71.8	1085	917	499	−73.821 094
$1\,^2E''(2\,^2B_1)$	1.717	55.9	1075	1055i[c]	917	−73.816 231
$1\,^4E'(1\,^4B_2)$	1.703	52.4	1272	939i[c]	880	−73.806 795
$1\,^4E'(1\,^4A_1)$	1.625	60.4	1145	2770i[c]	881	−73.799 771
$1\,^4A_1'(2\,^4A_1)$	1.624	60.0	1174	900	900	−73.780 854
$1\,^4A_2'(2\,^4B_2)$	1.621	60.0	1143	1262	1262	−73.770 926
B States	r_e (Å)	ω_s	ω_a	ω_π	ω_π (cm^{-1})[d]	E (a.u.)
$1\,^2\Pi_u$	1.561	848	1526	656	221	−73.837 058
$1\,^4\Pi_g$	1.551	876	1579	513	454	−73.833 854
$1\,^4\Sigma_u^-$	1.647	734	2379	75	75	−73.825 812

[a] D_{3h} and C_{2v} labels are used for each state to facilitate comparison with Fig. 3.
[b] ω_s, ω_a, and ω_b are the symmetric, asymmetric, and bending frequencies.
[c] Saddle points.
[d] ω_s and ω_a are defined as in Table III(A); ω_π are the two bending frequencies. The presence of Renner–Teller effects for degenerate states is seen in the removal of degeneracy of the ω_π frequencies.

III(B). The ground state of B_3 is of $^2A_1'$ symmetry at its triangular equilibrium geometry. This state correlates with a linear state of $^2\Pi_u$ symmetry, as shown in Fig. 3; this degenerate linear state also correlates with the first excited ($^2A_2''$) state, which also has a triangular equilibrium structure.

As detailed in Table IV, there is a saddle point on the ground state surface connecting the $^2A_1'$ minimum to the linear $^2\Pi_u$ minimum. This saddle lies only 619 cm^{-1} above the $^2\Pi_u$ state and has a zero-point energy (of course, excluding the imaginary-frequency mode) of 1245 cm^{-1}. The linear $^2\Pi_u$ state (with its zero-point energy of 1626 cm^{-1}) is therefore predicted to be marginally geometrically stable (by 238 cm^{-1}) and may even be metastable with respect to bending to produce the ground $1\,^2A_1'$ state.

There is also a saddle on the first excited $1\,^2A_2''$ state surface at the geometry indicated in Table IV. This saddle lies only 2740 cm^{-1} above the linear $^2\Pi_u$ state when zero-point corrections are taken into consideration. As stated above, the linear $^2\Pi_u$ state has its own zero-point energy of 1626 cm^{-1}; hence it is predicted to be geometrically stable

TABLE IV. Geometry, harmonic frequencies, and electronic energies of the transition states in the ground and first excited state surfaces $1\,^2A_1'(1\,^2A_1)$, $1\,^2A_2''(1\,^2B_1) \Leftrightarrow 1\,^2\Pi_u(1\,^2A_1, 1\,^2B_1)$. Barriers for interconversion to the isomeric forms.

States	r_e (Å)	θ	ω_s	ω_a	ω_b (cm^{-1})	E (a.u.)
$1\,^2A_1$	1.559	123	974	1515	269i	−73.834 239
$1\,^2B_1$	1.565	118	981	1349	241i	−73.829 880

Interconversion $A \rightarrow B$	Zero-point energy of A (cm^{-1})	Zero-point corrected barrier height (cm^{-1})[a]
$1\,^2A_1'(1\,^2A_1) \rightarrow 1\,^2\Pi_u(1\,^2A_1)$	1476	17 152
$1\,^2\Pi_u(1\,^2A_1) \rightarrow 1\,^2A_1'(1\,^2A_1)$	1626	1 864
$1\,^2A_2''(1\,^2B_1) \rightarrow 1\,^2\Pi_u(1\,^2B_1)$	1416	11 150
$1\,^2\Pi_u(1\,^2B_1) \rightarrow 1\,^2A_2''(1\,^2B_1)$	1626	2 740

[a] The barrier height is defined as the difference between the electronic energy of the transition state and the corresponding isomer with the zero-point energy of the transition state added on.

by 1114 cm^{-1} with respect to bending to form the $1\,^2A_2''$ state.

In addition to the two lowest-energy triangular states discussed above, our geometry calculations predict D_{3h} minima for all other nondegenerate states studied; the geometrical and harmonic vibrational parameters of these states are also detailed in Table III. In principle, these and the lowest two nondegenerate states could have displayed lower symmetry if second-order Jahn–Teller (SOJT) effects had been strong, but they did not.

In carrying out these studies of nonspatially degenerate states, FOJT distortion can not, of course, take place; nor do SOJT effects seem to be significant. However, artifactual symmetry breaking[8] (which results from difficulties that arise in solving the MCSCF equations) can lead to lower-symmetry electronic wave functions which, in turn, can exert artificial distortion forces on the molecule. For nondegenerate states, the configurations that enter into the MCSCF wave function do not belong to degenerate representations of the pertinent D_{3h} point group, but the orbitals appearing in these configurations may. To guarantee that the MCSCF wave function transforms as a representation of the D_{3h} point group at which the calculation is performed, it is therefore sufficient to restrict the orbitals to be of pure symmetry for both D_{3h} and C_{2v} symmetries from one MCSCF iteration to the next. This can be achieved by not permitting mixing among orbitals belonging to different irreducible representations of these groups.

B. Degenerate states at triangular geometries that FOJT distort

States that are degenerate at D_{3h} symmetry are subject to FOJT distortion. It is well known that such surfaces have the form of double cones in the neighborhood of the corresponding high symmetry point as depicted in Fig. 2(a). For D_{3h} species such as B_3, three pairs of equivalent minima and saddle points characterize the lower-energy surface as shown in Fig. 2(b). For all of the degenerate states studied, we calculated the geometries and vibrational frequencies of the minima and saddle points on the respective lower-energy surfaces; these findings are summarized in Table III.

We also calculated the pseudorotation barriers that connect each of the threefold minima through the threefold saddle points; these minima-to-saddle energy gaps are shown in Table V for each of the FOJT split states studied. To locate and characterize these stationary points, we used our potential energy surface walking algorithm. This tool also allowed us to move along the C_{2v}-breaking distortions that connect each of the above minima to their neighboring saddle points. In Table V, the zero-point energies of the corresponding minima (1284, 1326, and 1250 cm^{-1}) on the lower-energy surface are also given. These data, together with the zero-point corrected pseudorotation barriers (1885, 1268, and 2063 cm^{-1}, respectively), indicate that these states may be quite fluxional with respect to pseudorotation (the second such state is most likely to be very fluxional).

Proper treatment of symmetry within the electronic structure calculation on spatially degenerate states (at D_{3h} symmetry) which undergo FOJT distortion is handled, using the Utah MESS-KIT's HISYM program modules which constrain both the orbitals and configuration spaces to transform according to representations of the non-Abelian point group (and simultaneously to lower point groups). An additional source of artifactual symmetry breaking can arise in spatially degenerate cases. By using an MCSCF wave function whose configurations and corresponding amplitudes do not involve equal occupation of spatially degenerate orbitals, one can obtain unsymmetrical density matrices, which subsequently cause orbital degeneracies to be removed (artifactually). To avoid this problem,[9] the HISYM modules construct a wave function with equal configurational components along symmetry-equivalent blocks of the corresponding degenerate irreducible representation.

Once a distortion occurs and D_{3h} symmetry is lifted, artifactual symmetry breaking can be controlled, as discussed above for spatially nondegenerate states, by symmetry constraining the MCSCF orbitals. In these cases, C_{2v} symmetry is operative, so the orbitals must be constrained to remain of pure symmetry under C_{2v} symmetry from iteration to iteration within the MCSCF process; this will then ensure that the configurations will be of pure symmetry.

TABLE V. Barriers for pseudo-rotation of first-order Jahn–Teller unstable states.

States[a]	Zero-point corrected energy of the minimum (cm^{-1})	Zero-point corrected barrier height (cm^{-1})[b]
$1\,^4E''(1\,^4A_2,1\,^4B_1)$	1284	1881
$1\,^2E'(2\,^2A_1,1\,^2B_2)$	1327	1278
$1\,^2E''(1\,^2A_2,2\,^2B_1)$	1251	2063

[a] In parentheses we show the symmetry of the minimum and transition state, respectively. The zero point energy refers to the minimum.

[b] The barrier height is defined as the difference between the electronic energy of the transition state and the minimum with the zero-point energy of this transition state added on.

C. Linear states

As shown in Fig. 3, several low-lying linear states, which correlate to the low-energy triangular and bent states discussed earlier, were also examined in this work. The geometrical and harmonic vibrational parameters determined for these states are given in Table III(b). All of the states listed, including the Π states which are spatially degenerate, have real vibrational frequencies at linear structures and hence are locally geometrically stable (ignoring zero-point energies that may overcome barriers as discussed earlier for the ground $^2\Pi_u$ state). In contrast to degenerate states at bent geometries, linear spatially degenerate states can be geometrically stable because they are not subject to FOJT distortion. In fact, the two linear degenerate states studied ($^2\Pi_u$ and $^4\Pi_g$) were found to have $D_{\infty h}$ local minima; in these cases, Renner–Teller effects lead to splitting of the degenerate bending frequencies, as given in Table III, but neither frequency becomes complex.

For linear degenerate states, proper treatment of symmetry within the electronic structure calculation is again

handled using the Utah MESS-KIT's HISYM program modules. These tools constrain both the orbitals and configuration spaces to transform according to representations of the $D_{\infty h}$ point group (and simultaneously to lower point groups). Doing so guarantees that the electronic wave function remains of pure symmetry from one MCSCF iteration to another.

D. Comparison with earlier work

The first theoretical study of B_3 dates to the work of Whiteside[10(a)] on beryllium and boron clusters. Using unrestricted Hartree–Fock (UHF) calculations to optimize geometries and UHF-based fourth-order perturbation theory (UMP4) to treat correlation, they found a $1\,^2A_1'$ ground state for B_3, and they investigated the low-lying $1\,^4A_2$ state. Another study of linear boron clusters[10(b)] gave electronic energies and geometries of 11 states within a configuration interaction (CI) method. Our calculations predict the same linear ground state and first two excited states as proposed in this earlier work.

The thermochemical stabilities[10(c)] of a few pure and mixed boron and nitrogen clusters were studied using *ab initio* methods in order to investigate the presence of the corresponding cluster cations in the mass spectra of boron nitride. One triangular state of $1\,^2A_1'$ symmetry, two bent states of $^4A_2$ and $^4B_1$ symmetries and two linear states of $1\,^4\Pi_g$ and $1\,^2\Pi_g$ symmetry were studied. Geometry optimization was performed at the unrestricted SCF level and correlation was included through fourth order in perturbation theory (MP4) and by using the coupled-cluster method with double excitations including estimates of amplitudes of single and triple excitations (CCD-ST). Good agreement of our results with those obtained in this earlier research is found. Our term energies are comparable to the best estimates of these earlier workers. The geometries and frequencies that are obtained are quite similar to the earlier results for the triangular and bent states. However, for the $^4\Pi_g$ state, the earlier workers observed an artifactual negative curvature along the asymmetric stretch direction; we have not detected such an artifact in the present calculations.

V. OTHER RESULTS OF THIS WORK

A. Vertical spectroscopic transitions

1. Electric dipole and vibronically allowed transitions

Electric dipole transitions from the equilateral triangle ground $^2A_1'$ state to any $^2A_2''$ and $^2E'$ states are allowed; our calculations indicate that there are three such states (vertically lying approximately 7000 to 27 000 cm^{-1} above the ground state). Vibronically allowed transitions to $^2E''$ states (vertically lying approximately 26 000 and 40 000 cm^{-1} above the ground state) should also be considered. Vertical excitation energies for the lowest such states are given in Table VI and local harmonic vibrational frequencies of the corresponding states are provided in Table III; here the states are labeled according to D_{3h} symmetry because the vertical photon-induced excitation process occurs predominantly near such geometries.

TABLE VI. Lowest few CASSCF vertical excitation energies.

Transition type	State[a]	T_e (cm^{-1})[b]
	$1\,^2A_1'(1\,^2A_1)$	0
Dipole allowed	$1\,^2A_2''(1\,^2B_1)$	7 082
Dipole allowed	$1\,^2E'(2\,^2A_1,1\,^2B_2)$	15 085
Dipole allowed	$2\,^2E'(3\,^2A_1,2\,^2B_2)$	27 308
Vibronically allowed	$1\,^2E''(1\,^2A_2,2\,^2B_1)$	26 594
Vibronically allowed	$2\,^2E''(2\,^2A_2,3\,^2B_1)$	38 918

[a] D_{3h} and C_{2v} labels are used for each state to facilitate comparison with Fig. 3.

[b] The $^2E'$ excitation energies were obtained as configuration interaction (CI) eigenvalues in the CASSCF optimization of the $1\,^2A_1'$ state (both symmetries appear as A_1 in C_{2v} symmetry). Similarly, the $^2E''$ excitation energies were obtained as CI roots in the CASSCF optimization of the $1\,^2A_2''$ state (both symmetries appear as B_1 in C_{2v} symmetry).

2. Transitions to Jahn–Teller distorted states

The lowest excited states of $^2E'(2\,^2A_1,1\,^2B_2)$ and $^2E''(1\,^2A_2,2\,^2B_1)$ symmetries (for which our calculations have provided information about the geometries, energies, and vibrational frequencies of the minima and saddle points associated with the FOJT-split states) are amenable to spectroscopic study. The low barriers to pseudorotation for both of these states should provide clearly discernable features in vibrationally resolved spectra.

3. Transitions originating from linear structures

As already mentioned when discussing the properties of the ground state surface, we expect the linear $^2\Pi_u$ state to be marginally geometrically stable or even metastable when zero-point energies are included (in which case, it could interconvert to the triangular $1\,^2A_1'$ global minimum or to the first excited $1\,^2A_2''$ state). As a result, it will be unlikely that spectroscopic transitions originating at linear geometries will be observed even in sources energetic enough to produce linear species.

B. B_3 dissociation energy

The dissociation energy of the ground state of B_3 to produce B and B_2 in their respective ground states was calculated using a CASSCF wave function which properly dissociates to diatomic and atomic fragments. We obtain a value of $D_e = 4.96$ eV, which shows the boron trimer is approximately two times more strongly bound than is the aluminum trimer ($\leqslant 2.40$ eV).[2] Experimentally it has been confirmed that boron cluster cations are 2–3 times more strongly bound than their aluminum homologs.[1(a)] Our B_3 dissociation energy is comparable to that obtained in the purely *ab initio* MP4 (4.86 eV) and CCD-ST (4.87 eV) studies of Ref. 10(c). Based on experience that CCD-ST calculations underestimate dissociation energies, the authors of Ref. 10(c) used a scaling factor to obtain an estimate of the B_3 dissociation energy of 5.60 eV, which is 0.64 eV larger than ours.

C. Ionization potential and the B_3 cation

We find a triangular $^1A_1'$ state to be the ground state for the B_3^+ cation; its main configuration is obtained by removing an electron from the $5a_1$ orbital of the $^2A_1'$ neutral ground state (see Table VII). The Koopmans' theorem estimate of the corresponding ionization potential (IP) is 9.44 eV, and the CASSCF-based IP is 8.74 eV. The orbital relaxation energy (e.g., the difference between the Koopmans' estimate and the SCF-level estimate) was found to be ten times larger than the correlation correction (the difference between the CASSCF estimate and the SCF estimate). We expect correlation corrections to increase the predicted IP beyond the CASSCF value when higher levels of correlation are included, but we anticipate that such improvements in the treatment of correlation will not increase the IP beyond the Koopmans' value. Earlier configuration interaction calculations[10(d)] yielded IPs in the range 8.5–9.5 eV for B_3.

VI. SUMMARY

The ground state of B_3 is of $^2A_1'$ symmetry at its triangular equilibrium geometry. The first excited ($^2A_2''$) state also has a triangular equilibrium structure. There is a saddle point on the ground state surface connecting the $^2A_1'$ minimum to the linear $^2\Pi_u$ minimum to which it adiabatically correlates. This saddle lies only 238 cm^{-1} above the linear minimum when zero-point energies are taken into consideration. As a result, the linear structure may be metastable with respect to bending to produce the ground $1\,^2A_1'$ state.

Our geometry calculations predict D_{3h} minima for all other nondegenerate states studied. For all of the spatially degenerate states studied, all of which undergo first-order Jahn–Teller distortion, we calculated the geometries and vibrational frequencies of the threefold minima and saddle points on the double cone's lower-energy surface. We also calculated the pseudorotation barriers that connect each of the threefold minima through the threefold saddle points. Our data, including zero-point corrected pseudorotation barriers indicate that the Jahn–Teller distorted states may be quite fluxional with respect to pseudorotation.

Three electric dipole allowed transitions from the equilateral triangle ground $^2A_1'$ state to $^2A_2''$ and $^2E'$ states are predicted in the range 7000 to 27 000 cm^{-1} above the ground state. Vibronically allowed transitions to $^2E''$ states (vertically lying approximately 26 000 and 40 000 cm^{-1} above the ground state) are also predicted. The metastability of the lowest energy linear structure renders it unlikely that spectroscopic transitions originating at linear geometries will be observed even when using energetic sources.

The dissociation energy of the ground state of B_3 is predicted to be $D_e = 4.96$ eV. For the B_3^+ cation, we predict a triangular $^1A_1'$ structure and an ionization potential (IP) based on our CASSCF calculation of 8.74 eV.

TABLE VII. Main electronic configurations for the low-lying states of B_3.[a]

$1\,^2A_1'(1\,^2A_1)$	0.88	$1a_1^2 2a_1^2 1b_2^2 3a_1^2 2b_2^2 4a_1^2 1b_2^2 5a_1^1$
	−0.11	$1a_1^2 2a_1^2 1b_2^2 3a_1^2 2b_2^1 4a_1^1 1b_2^1 5a_1^2 3b_2^1$
$1\,^2A_2''(1\,^2B_1)$	0.87	$1a_1^2 2a_1^1 1b_2^2 3a_1^2 2b_2^2 4a_1^2 5a_1^2 1b_2^1$
	0.19	$1a_1^2 2a_1^2 1b_2^2 3a_1^2 2b_2^2 4a_1^2 1b_2^1 3b_2^2$
$1\,^4E''(1\,^4A_2)$	0.92	$1a_1^2 2a_1^2 1b_2^2 3a_1^2 2b_2^2 4a_1^2 3b_2^1 1b_2^1 5a_1^1$
	0.16	$1a_1^2 2a_1^2 1b_2^2 3a_1^2 2b_2^2 6a_1^2 3b_2^1 1b_2^1 5a_1^1$
$1\,^4E''(1\,^4B_1)$	0.91	$1a_1^2 2a_1^2 1b_2^2 3a_1^2 2b_2^2 4a_1^2 1b_2^1 5a_1^1 6a_1^1$
	0.14	$1a_1^2 2a_1^2 1b_2^2 3a_1^2 2b_2^1 4a_1^2 1b_2^1 5a_1^2 3b_2^1$
$1\,^2E'(2\,^2A_1)$	0.74	$1a_1^2 2a_1^2 1b_2^2 3a_1^2 2b_2^2 4a_1^2 1b_2^2 6a_1^1$
	0.37	$1a_1^2 2a_1^2 1b_2^2 3a_1^2 2b_2^2 4a_1^1 1b_2^2 5a_1^2$
$1\,^2E'(1\,^2B_2)$	0.81	$1a_1^2 2a_1^2 1b_2^2 3a_1^2 2b_2^2 4a_1^2 1b_2^2 3b_2^1$
	−0.32	$1a_1^2 2a_1^2 1b_2^2 3a_1^2 2b_2^1 4a_1^2 1b_2^2 5a_1^2$
$1\,^2E''(1\,^2A_2)$	0.80	$1a_1^2 2a_1^2 1b_2^2 3a_1^2 2b_2^2 4a_1^2 3b_2^1 1b_2^1 5a_1^1$
	0.47	$1a_1^2 2a_1^2 1b_2^2 3a_1^2 2b_2^2 4a_1^2 3b_2^1 1b_2^1 5a_1^1$
$1\,^2E''(2\,^2B_1)$	0.90	$1a_1^2 2a_1^2 1b_2^2 3a_1^2 2b_2^2 4a_1^2 5a_1^1 1b_2^1 6a_1^1$
	−0.13	$1a_1^2 2a_1^2 1b_2^2 3a_1^2 4a_1^2 3b_2^2 1b_2^1 5a_1^1 6a_1^1$
$1\,^4E'(1\,^4A_1)$	0.57	$1a_1^2 2a_1^2 1b_2^2 3a_1^2 2b_2^1 4a_1^2 1b_2^2 5a_1^1 3b_2^1$
	−0.53	$1a_1^2 2a_1^2 1b_2^2 3a_1^2 2b_2^2 4a_1^1 1b_2^2 5a_1^1 6a_1^1$
$1\,^4E'(1\,^4B_2)$	0.86	$1a_1^2 2a_1^2 1b_2^2 3a_1^2 2b_2^1 4a_1^2 1b_2^2 5a_1^1 6a_1^1$
	−0.19	$1a_1^2 2a_1^2 1b_2^2 3a_1^2 2b_2^1 4a_1^1 1b_2^2 5a_1^2 6a_1^1$
$1\,^4A_1'(1\,^4A_1)$	0.62	$1a_1^2 2a_1^2 1b_2^2 3a_1^2 2b_2^1 4a_1^2 1b_2^2 5a_1^1 3b_2^1$
	0.62	$1a_1^2 2a_1^2 1b_2^2 3a_1^2 2b_2^2 4a_1^1 1b_2^2 5a_1^1 6a_1^1$
$1\,^4A_2'(2\,^4B_2)$	0.65	$1a_1^2 2a_1^2 1b_2^2 3a_1^2 2b_2^1 4a_1^2 1b_2^2 5a_1^1 6a_1^1$
	0.65	$1a_1^2 2a_1^2 1b_2^2 3a_1^2 2b_2^2 4a_1^1 1b_2^2 5a_1^1 3b_2^1$
$1\,^2\Pi_u$	0.46	$1a_1^2 2a_1^2 1b_2^2 3a_1^2 2b_2^2 4a_1^2 1b_2^2 5a_1^1$
	0.46	$1a_1^2 2a_1^2 1b_2^2 3a_1^2 2b_2^2 4a_1^2 5a_1^2 1b_2^1$
$1\,^4\Pi_g$	0.61	$1a_1^2 2a_1^2 1b_2^2 3a_1^2 2b_2^2 4a_1^1 3b_2^1 1b_2^1 5a_1^2$
	0.61	$1a_1^2 2a_1^2 1b_2^2 3a_1^2 2b_2^2 4a_1^1 3b_2^1 1b_2^2 5a_1^1$
$1\,^4\Sigma_u^-$	0.85	$1a_1^2 2a_1^2 1b_2^2 3a_1^2 2b_2^2 4a_1^2 3b_2^1 1b_2^1 5a_1^1$
	0.26	$1a_1^2 2a_1^2 1b_2^2 3a_1^2 2b_2^2 4a_1^1 3b_2^2 1a_2^2 5a_1^1$

[a] The numbers in the left column are the configuration interaction coefficients.

ACKNOWLEDGMENTS

This work was supported by National Science Foundation Grant No. CHE 8814765, and in part by the Office of Naval Research. R. H. wishes to thank Dr. Maciej Gutowski for his many helpful suggestions and encouragement and Professor Michael Morse for many stimulating conversations about the spectroscopy of clusters.

[1] (a) L. Hanley and S. Anderson, J. Phys. Chem. **91**, 5161 (1987); (b) **89**, 2848 (1988).

[2] Z. Fu, G. Lemire, Y. Hamrick, S. Taylor, J. Shui, and M. Morse, J. Chem. Phys. **88**, 3524 (1988).

[3] T. H. Dunning, J. Chem. Phys. **90**, 1007 (1989).

[4] K. P. Huber and G. Herzberg, *Molecular Spectra and Molecular Structure, IV. Constants of Diatomic Molecules* (Van Nostrand Reinhold, New York, 1979).

[5] M. Dupuis and B. Liu, J. Chem. Phys. **68**, 2902 (1978).

[6] J. Nichols, H. Taylor, P. Schmidt, and J. Simons, J. Chem. Phys. **92**, 340 (1990).

[7] The Utah MESS-KIT is a suite of highly modular codes that were programmed in-house to give a variety of electronic structure functionalities by J. A. Nichols, M. R. Hoffmann, R. A. Kendall, H. L. Taylor, D. W. O'Neal, E. Earl, R. Hernandez, M. Gutowski, J. Boatz, K. Bak, J. Anchell, X. Wang, M. Feyereisen, and J. Simons.

[8] A review on real vs artifactual symmetry breaking has been given in, E. Davidson and W. Borden, J. Phys. Chem. **87**, 4785 (1983).

[9] E. Earl, J. Comp. Chem. **11**, 636 (1990).

[10] (a) R. A. Whiteside, PhD. thesis, Carnegie Mellon University, Pittsburgh, Pennsylvania 1981; (b) A. Pellegatti, F. Marinelli, M. Roche, D. Maynau, and J. Malrieu, J. Phys. **48**, 29 (1987); (c) J. Martin, J. Francois, R. Gijbels, J. Chem. Phys. **90**, 6469 (1989); (d) L. Hanley, J. Whitten, and S. Anderson, J. Phys. Chem. **92**, 5803 (1988).